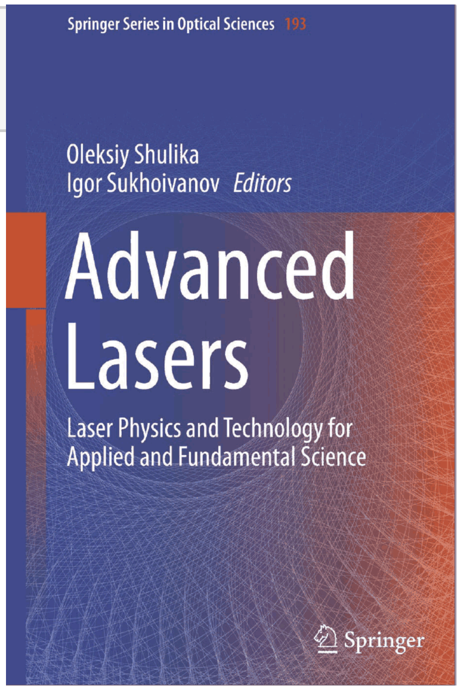

ISSN 0342-4111 ISSN 1556-1534 (electronic)
Springer Series in Optical Sciences
ISBN 978-94-017-9480-0 ISBN 978-94-017-9481-7 (eBook)
DOI 10.1007/978-94-017-9481-7

Chapter 8

Advanced Lasers
Volume 193 of the series Springer Series in Optical Sciences pp 117-146

Date: 29 April 2015

Optical Processors as Conceptual Tools for Designing Nonconventional Devices

Jorge Ojeda-Castañeda, Sergio Ledesma, Emmanuel Yépez-Vidal, Cristina M. Gomez-Sarabia, Miguel Torres-Cisneros

Abstract

We discuss the use of nonconventional optical processors for generating irradiance distributions, which are useful for visualizing the characteristics of imaging devices that extend the depth of field. Our discussion starts with the use of binary masks for generating nonconventional irradiance distributions, which display the variations of the impulse response with focus errors. By using an anamorphic optical processor these irradiance distributions can easily be transformed into variations of the optical transfer function vs focus errors. Next, another anamorphic optical processor is used for generating the ambiguity function of a pupil aperture, which helps to visualize the variations of the optical transfer function with variable focus error. Finally, we translate the integral transform associated with the evaluation of the ambiguity function into tunable devices for controlling the depth of field, without modifying the size of the pupil aperture.

Keywords

Imaging devices Optical processors Optical visualization Extended depth of field Pupil engineering Apodization Phase-only masks Ambiguity function Wigner distribution Phase-space optics

Table of contents

Springer Series in Optical Sciences 193

Oleksiy Shulika
Igor Sukhoivanov *Editors*

Advanced Lasers

Laser Physics and Technology for Applied and Fundamental Science

Springer

Springer Series in Optical Sciences

Volume 193

Springer Series in Optical Sciences is led by Editor-in-Chief William T. Rhodes, Georgia Institute of Technology, USA, and provides an expanding selection of research monographs in all major areas of optics:

- lasers and quantum optics
- ultrafast phenomena
- optical spectroscopy techniques
- optoelectronics
- information optics
- applied laser technology
- industrial applications and
- other topics of contemporary interest.

With this broad coverage of topics the series is useful to research scientists and engineers who need up-to-date reference books.

More information about this series at http://www.springer.com/series/624

Oleksiy Shulika • Igor Sukhoivanov
Editors

Advanced Lasers

Laser Physics and Technology for Applied and Fundamental Science

Springer

Editors
Oleksiy Shulika
Universidad de Guanajuato
Salamanca
Mexico

Igor Sukhoivanov
Universidad de Guanajuato
Salamanca
Mexico

ISSN 0342-4111 ISSN 1556-1534 (electronic)
Springer Series in Optical Sciences
ISBN 978-94-017-9480-0 ISBN 978-94-017-9481-7 (eBook)
DOI 10.1007/978-94-017-9481-7

Library of Congress Control Number: 2014958008

Springer Dordrecht Heidelberg New York London

Printed on acid-free paper

Springer is part of Springer Science+Business Media (www.springer.com)

Contents

Contributors

Alexander Alexandrov Adaptive Optics Lab, Moscow State Technical University (MAMI), Moscow, Russia

E. Alvarado-Méndez Departamento de Ingeniería Electrónica, División de Ingenierías Campus Irapuato Salamanca, Universidad de Guanajuato, Salamanca, GTO, México

Valerio Annovazzi-Lodi Department of Electrical, Computer and Biomedical Engineering, University of Pavia, Pavia, Italy

José E. Antonio-Lopez CREOL The College of Optics and Photonics, University of Central Florida, Orlando, FL, USA

A. A. Belyanin Department of Physics and Astronomy, Texas A & M University, College Station TX, USA

O. N. Bezkrovnaya Institute for Single Crystals, SSI "Institute for Single Crystals", National Academy of Sciences of Ukraine, Kharkiv, Ukraine

Vladimir L. Derbov Department of Physics, Saratov State University, Saratov, Russia

Silvano Donati Department of Electrical, Computer and Biomedical Engineering, University of Pavia, Pavia, Italy

Julián M. Estudillo-Ayala Cuerpo Académico de Optoelectrónica, DICIS Universidad de Guanajuato, Guanajuato, Mexico

F. Gómez-Aguilar Departmento de Materiales Solares, Instituto de Energías Renovables, Universidad Nacional Autónoma de México, Temixco, MOR, México

Cristina M. Gómez-Sarabia Digital Arts Department, Engineering Division, Campus Salamanca, University of Guanajuato, Guanajuato, Mexico

S. V. Gagarsky Mechanics and Optics, Saint Petersburg National Research University of Information Technologies, Saint-Petersburg, Russia

Chunlei Guo The Institute of Optics, University of Rochester, Rochester, NY, USA

Yu. A. Gurkalenko Institute for Single Crystals, SSI "Institute for Single Crystals", National Academy of Sciences of Ukraine, Kharkiv, Ukraine

Juan C. Hernandez Garcia Instituto Nacional de Astrofisica Optica y Electronica, Puebla, Mexico

Daniel Jauregui-Vazquez Cuerpo Académico de Optoelectrónica, DICIS Universidad de Guanajuato, Guanajuato, Mexico

Hitoshi Kawaguchi Graduate School of Materials Science, Nara Institute of Science and Technology, Ikoma, Nara, Japan

V. I. Kislov Prokhorov General Physics Institute, Russian Academy of Science, Moscow, Russia

V. V. Kiyko Prokhorov General Physics Institute, Russian Academy of Science, Moscow, Russia

E. R. Kocharovskaya IAP RAS, Nizhny Novgorod, Russia

V. V. Kocharovsky IAP RAS, Nizhny Novgorod, Russia

Department of Physics and Astronomy, Texas A & M University, College Station TX, USA

Vl. V. Kocharovsky IAP RAS, Nizhny Novgorod, Russia

V. A. Kondratyev Prokhorov General Physics Institute, Russian Academy of Science, Moscow, Russia

Alexis Kudryashov Adaptive Optics Lab, Moscow State Technical University (MAMI), Moscow, Russia

Sergio Ledesma Electronics Department, Engineering Division, Campus Salamanca, University of Guanajuato, Guanajuato, Mexico

P. LiKamWa CREOL The College of Optics and Photonics, University of Central Florida, Orlando, FL, USA

A. V. Lopin Institute for Single Crystals, SSI "Institute for Single Crystals", National Academy of Sciences of Ukraine, Kharkiv, Ukraine

V. V. Maslov O. Ya. Usikov Institute for Radiophysics and Electronics, National Academy of Sciences of Ukraine, Kharkiv, Ukraine

Daniel A. May-Arrioja Fiber and Integrated Optics Laboratory, UAMRR Universidad Autónoma de Tamaulipas, Reynosa, TAMPS, México

E. N. Ofitserov Prokhorov General Physics Institute, Russian Academy of Science, Moscow, Russia

Jorge Ojeda-Castañeda Electronics Department, Engineering Division, Campus Salamanca, University of Guanajuato, Guanajuato, Mexico

A. G. Plaksiy Institute for Single Crystals, SSI "Institute for Single Crystals", National Academy of Sciences of Ukraine, Kharkiv, Ukraine

S. V. Pogorelov National University of Pharmacy, Kharkov, Ukraine

I. M. Pritula Institute for Single Crystals, SSI "Institute for Single Crystals", National Academy of Sciences of Ukraine, Kharkiv, Ukraine

V. M. Puzikov Institute for Single Crystals, SSI "Institute for Single Crystals", National Academy of Sciences of Ukraine, Kharkiv, Ukraine

Roberto Rojas-Laguna Cuerpo Académico de Optoelectrónica, DICIS Universidad de Guanajuato, Guanajuato, Mexico

Alexey Rukosuev Adaptive Optics Lab, Moscow State Technical University (MAMI), Moscow, Russia

Nataliya Sakhnenko Kharkiv National University of Radio Electronics, Kharkiv, Ukraine

Institute of Radio Physics and Electronics NASU, Kharkiv, Ukraine

Vadim Samarkin Adaptive Optics Lab, Moscow State Technical University (MAMI), Moscow, Russia

José J. Sanchez-Mondragón Instituto Nacional de Astrofisica, Óptica y Electrónica, Tonantzintla, PUE, México

A. N. Sergeev Mechanics and Optics, Saint Petersburg National Research University of Information Technologies, Saint-Petersburg, Russia

Tatyana A. Sergeeva Department of Physics, Saratov State University, Saratov, Russia

Vladislav V. Serov Department of Physics, Saratov State University, Saratov, Russia

Juan M. Sierra Hernandez Cuerpo Académico de Optoelectrónica, DICIS Universidad de Guanajuato, Guanajuato, Mexico

A. G. Suzdaltsev Prokhorov General Physics Institute, Russian Academy of Science, Moscow, Russia

Miguel Torres-Cisneros Electronics Department, Engineering Division, Campus Salamanca, University of Guanajuato, Guanajuato, Mexico

A. Y. Vorobyev The Institute of Optics, University of Rochester, Rochester, NY, USA

Emmanuel Yépez-Vidal Electronics Department, Engineering Division, Campus Salamanca, University of Guanajuato, Guanajuato, Mexico

Chapter 8
Optical Processors as Conceptual Tools for Designing Nonconventional Devices

Jorge Ojeda-Castañeda, Sergio Ledesma, Emmanuel Yépez-Vidal, Cristina M. Gómez-Sarabia and Miguel Torres-Cisneros

Abstract We discuss the use of nonconventional optical processors for generating irradiance distributions, which are useful for visualizing the characteristics of imaging devices that extend the depth of field. Our discussion starts with the use of binary masks for generating nonconventional irradiance distributions, which display the variations of the impulse response with focus errors. By using an anamorphic optical processor these irradiance distributions can easily be transformed into variations of the optical transfer function vs focus errors. Next, another anamorphic optical processor is used for generating the ambiguity function of a pupil aperture, which helps to visualize the variations of the optical transfer function with variable focus error. Finally, we translate the integral transform associated with the evaluation of the ambiguity function into tunable devices for controlling the depth of field, without modifying the size of the pupil aperture.

8.1 Introduction

In image science, the word apodization is used for describing a large set of techniques for shaping the Point Spread Function (PSF) of an optical system. However, the word apodization [1–6] was coined in optical spectroscopy for describing the use of tapered 1-D pupil masks that reduce diffraction bands, or optical side lobes, on the PSF. It was recognized that this type of tapering masks also expand the width of the PSF, while reducing the presence of the side lobes. These two previous features are useful for extending the axial PSF of a 2-D, radially symmetric optical systems [7–9]. For this type of applications, it is convenient to recognize that the normalized version of the axial PSF expresses the Strehl ratio vs focus error [10].

J. Ojeda-Castañeda (✉) · S. Ledesma · E. Y.-Vidal · M. T.-Cisneros
Electronics Department, Engineering Division, Campus Salamanca, University of Guanajuato, Guanajuato, Mexico
e-mail: jojedacas@ugto.mx

C. M. Gomez-Sarabia
Digital Arts Department, Engineering Division, Campus Salamanca, University of Guanajuato, Guanajuato, Mexico

O. Shulika, I. Sukhoivanov (eds.), *Advanced Lasers*,
Springer Series in Optical Sciences 193, DOI 10.1007/978-94-017-9481-7_8

Of course, one can extend the depth of field of an imaging device, simply by closing down the pupil aperture or by using annular pupil apertures. However, these solutions reduce the resolution as well as the light gathering power of the optical system. Hence, there is an optical engineering endeavor that aims to reduce the influence of focus errors on the optical transfer function (OTF), without substantially reducing either the resolution or the light gathering power of an optical system [11–14].

In Sect. 8.2, we discuss the use of binary masks that have unit transmittance only along a very narrow slit, which follows suitable paths for generating optical path differences [15–18].

In Sect. 8.3, we show that a display of the ambiguity function [19–23] is rather useful diagram for visualizing the impact of focus error on the OTF. The ambiguity function of the pupil aperture exhibits (in a single picture) the influence of focus error on the OTF. Furthermore, the ambiguity function helps to expand the defocused OTF as a Taylor series expansion in terms of the focus error coefficient. Half of the terms of the Taylor series can be reduced to zero if the complex amplitude transmittance of the pupil aperture is a hermitian function. Hence, one needs to explore the use of masks whose amplitude variations are described by even functions, while the phase variations are described by odd functions [24].

By using a suitable mask one can obtain an OTF that does not have zero values inside the passband, and the OTF varies slowly with focus errors. Thus, one can preserve the spatial frequency content of several planar images, which are located at different depths. These images are recorded with virtually the same amount of contrast reduction. Consequently, one can use the same digital filter for restoring the contrast of all recorded images [25].

The present technology allows producing nonconventional masks, with complex amplitude transmittance. Furthermore, there several fast digital algorithms for improving the quality of an image. Hence, nowadays one can use both nonconventional devices with complex amplitude transmittance, as well as fast digital algorithms for extending the depth of field [26–31].

In Sect. 8.4, we show that the schematics of an optical processor are useful for gaining physical insights, on the design of tunable devices for controlling the depth of field. To this end, we translate the integral transform associated with the evaluation of the ambiguity function into tunable devices for controlling the depth of field, without modifying the pupil aperture. These types of devices are here denoted as Alvarez-Lohmann lenses. In Sect. 8.5, we summarize our contribution.

8.2 Visualizing a PSF with High Depth of Focus

We start by writing Helmholtz differential equation that describes the propagation of a 2-D scalar wave φ(x, z). That is,

$$[\partial_x^2 + \partial_z^2 + k^2]\varphi(x,\ z) = 0. \tag{8.1}$$

In Eq. (8.1) the wave number is denoted as $k = 2\pi/\lambda$. It is easy to verify that its formal solution is

$$\varphi(x, z) = \exp\left[ikz\sqrt{k^{-2}\partial_x^2 + 1}\right]\varphi(x, 0). \tag{8.2}$$

The exponential operator in Eq. (8.2) is to be used as a power series expansion of the differential operator ∂_x^2. See for example references from 32 to 34. One can relate the formal solution in Eq. (8.2) to the angular spectrum of planes waves, by assuming that the initial condition $\varphi(x, z = 0)$ can be expressed as the inverse Fourier transform of the plane wave spectrum $\Phi(\mu)$. That is,

$$\varphi(x, 0) = \int_{-\infty}^{\infty} \Phi(\mu)\exp(i2\pi x\mu)d\mu \tag{8.3}$$

In Eq. (8.3) we use the Greek letter μ for denoting the spatial frequency along the horizontal axis, which is of course related to direction cosine along the horizontal axis α as follows, $\mu = \alpha/\lambda$. If one applies the exponential operator in Eq. (8.2) to the inverse Fourier transform in Eq. (8.3) one obtains

$$\begin{aligned}&\exp\left[ikz\sqrt{k^{-2}\partial_x^2 + 1}\right]\varphi(x,\ 0)\\ &= \int_{-\infty}^{\infty} \Phi(\mu)\exp[ikz\sqrt{1-\lambda^2\mu^2}]\exp(i2\pi x\mu)\ d\mu.\end{aligned} \tag{8.4}$$

As one should expect. The result in Eq. (8.4) can be usefully rewritten in the following manner. As is depicted in Fig. 8.1, let us assume that that in a classical optical processor the input is a pinhole size source, which is represented by the mathematical expression

$$u_0(x, z) = \delta(x)\delta(z). \tag{8.5}$$

As is depicted in Fig. 8.1, at the Fraunhofer plane with spatial frequency variables (μ, ζ), we place a mask with complex amplitude transmittance

$$\mathrm{P}(\mu, \zeta) = Q(\mu)\delta(\zeta - \sqrt{\Omega^2 - \mu^2}). \tag{8.6}$$

At this stage, we set $Q(\mu) = \mathrm{rect}(\mu/2\Omega)$ where the Greek letter Ω denotes the cut-off value of the spatial frequency μ. The second term in Eq. (8.6) describes a very narrow slit that follows the curve $\zeta = \sqrt{}(\Omega^2 - \mu^2)$. The amplitude impulse response of the coherent optical processor is

$$p(x, z) = \int_{-\infty}^{\infty}\int_{-\infty}^{\infty} \mathrm{P}(\mu, \zeta)exp[i2\pi(x\mu + z\zeta)]d\mu d\zeta \tag{8.7a}$$

Or equivalently, by using Eq. (8.6), one can write Eq. (8.7a) as

$$p(x, z) = \int_{-\infty}^{\infty} \mathrm{Q}(\mu)exp[i2\pi(x\mu + z\sqrt{\Omega^2 - \mu^2})]d\mu \tag{8.7b}$$

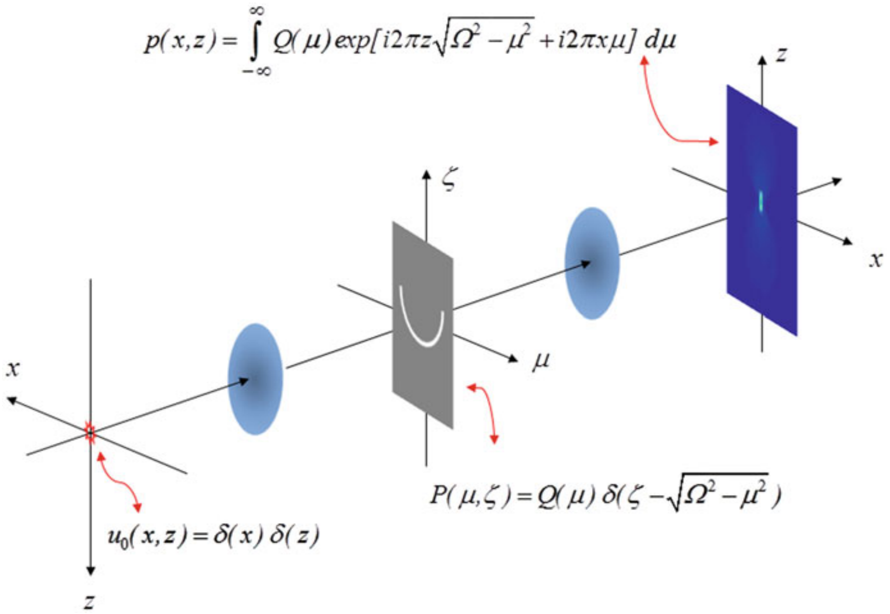

Fig. 8.1 Schematic diagram of an optical processor using a pupil mask in the form of narrow slit

By a simple comparison, between Eqs. (8.4) and (8.7b), it is apparent that the optical processor is able to display, in a single 2-D picture, the propagation the scalar wave $\varphi(x, z)$; where $\Omega = \lambda^{-1}$.

One can generalize this remarkably simple result by selecting the complex amplitude distribution, at the Fraunhofer plane, as

$$Q(\mu) = \Phi(\mu) rect\left(\frac{\mu}{2\lambda^{-1}}\right). \tag{8.8}$$

We discuss next other useful examples. In the paraxial regime, the propagation of a 2-D wave scalar wave $\varphi(x, z)$ can be is described using the differential equation

$$\left[\partial_x^2 + i2k\partial_z\right]\phi(x,z) = 0 \tag{8.9}$$

It is straightforward to show that for this case, as depicted in Fig. 8.2, on needs a mask with complex amplitude transmittance

$$\mathrm{P}(\mu,\zeta) = Q(\mu)\delta\left(\zeta + \frac{\mu^2}{2\Omega}\right); \tag{8.10}$$

where again $\Omega = \lambda^{-1}$. In Fig. 8.3 we show the irradiance distributions associated to the pictures describing the propagation of an initial point source, as predicted by Helmholtz equation; as well as the picture that portraits wave propagation within the paraxial approximation. It is interesting to note that the picture describing propagation in the paraxial regime (left hand side of Fig. 8.3) has a wider diverging angle

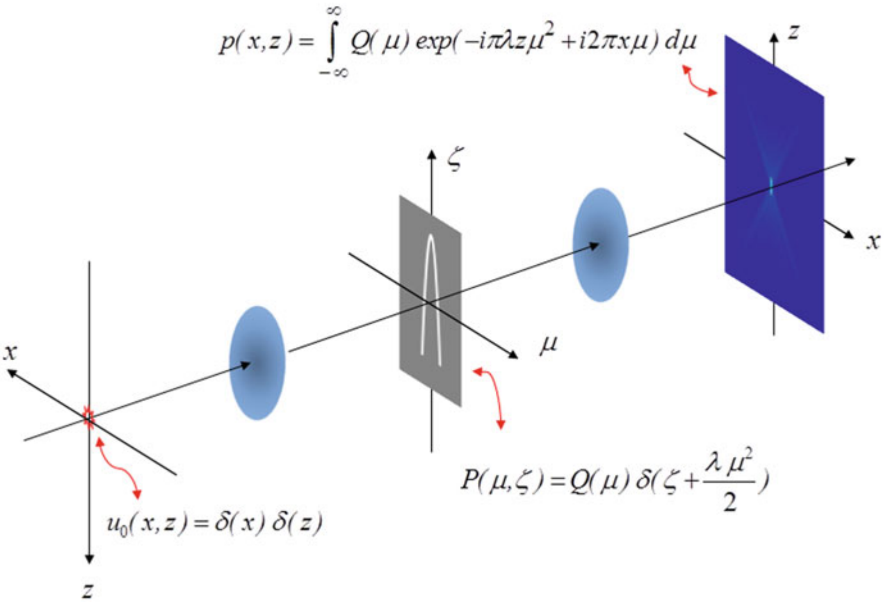

Fig. 8.2 Optical processor used for visualizing the propagation of a 2-D scalar wave, in the paraxial regime

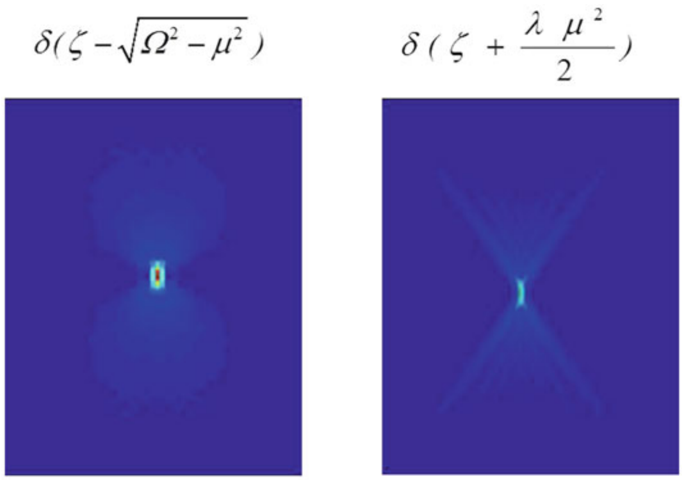

Fig. 8.3 Irradiance distributions displaying the impulse response at the (x, z) plane

than the picture describing propagation according to Helmholtz equation (right hand side of Fig. 8.3).

Next, we discuss an interesting variant of our previous results. As depicted in Fig. 8.4, let us assume that the mask has the following complex amplitude transmittance

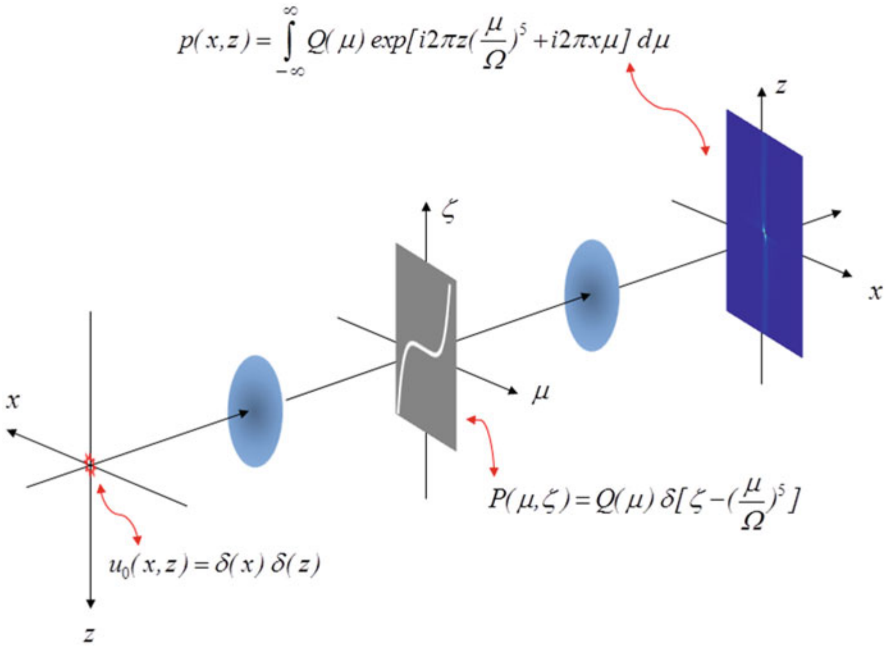

Fig. 8.4 Optical processor using a pupil mask in the form of narrow slit, which follows a fifth power curve

$$\mathrm{P}(\mu,\zeta) = Q(\mu)\delta\left[\zeta - \sigma\left(\frac{\mu}{\Omega}\right)^5\right]. \tag{8.11}$$

At the output plane of the coherent optical processor, the complex amplitude distribution is

$$p(x,\ z) = \int_{-\infty}^{\infty} \mathrm{Q}(\mu) exp\left\{i2\pi\left[x\mu + z\sigma\left(\frac{\mu}{\Omega}\right)^5\right]\right\} d\mu\ . \tag{8.12}$$

The complex amplitude distribution in Eqs. (8.11) and (8.12) have now the following interpretation.

At the Fraunhofer plane the curve $\zeta = (\mu/\Omega)^5$ represents a phase profile to the fifth power. Hence, now at the output plane, the z-axis denotes the maximum value of the optical path difference, which is reached at the edge ($\mu = \pm\Omega$) of the 1-D pupil aperture. Again the pupil aperture is described by the function rect($\mu/2\Omega$). Consequently, in this later example, the variable ζ is a dimensionless variable. Its Fourier transform pair is the dimensionless variable

$$z = (N-1)\frac{t}{\lambda} \tag{8.13}$$

Table 8.1 Possible curve for the narrow slit in the Fraunhofer plane. The displays that are described along the third column are obtained using the optical processor in Fig. 8.1. And the displays along the third column are obtained using the optical processor in Fig. 8.6.

Describing	Binary Mask	Display 1	Display 2
Nonparaxial propagation	$P(\mu,\zeta) = Q(\mu)\delta(\zeta - \sqrt{\Omega^2 - \mu^2})$	PSF along the Z-axis	MTF along the Z-axis
Paraxial propagation	$P(\mu,\zeta) = Q(\mu)\delta\left(\zeta + \frac{\mu^2}{2\Omega}\right)$	PSF along the Z-axis	MTF along the Z-axis
Asymmetric quadratic phase mask	$P(\mu,\zeta) = Q(\mu)\delta\left[\zeta - \operatorname{sgn}(\mu)\left(\frac{\mu}{\Omega}\right)^2\right]$	PSF vs OPD	MTF vs OPD
Cubic phase mask	$P(\mu,\zeta) = Q(\mu)\delta\left[\zeta - \left(\frac{\mu}{\Omega}\right)^3\right]$	PSF vs OPD	MTF vs OPD
Fractional wavefront	$P(\mu,\zeta) = Q(\mu)\delta\left[\zeta - \operatorname{sgn}(\mu)\left\lvert\frac{\mu}{\Omega}\right\rvert^{3.75}\right]$	PSF vs OPD	MTF vs OPD
High order phase mask	$P(\mu,\zeta) = Q(\mu)\delta\left[\zeta - \left(\frac{\mu}{\Omega}\right)^5\right]$	PSF vs OPD	MTF vs OPD

Hence, as is indicated in Eq. (8.13), the Latin letter z describes the variation of optical path difference of an optical element. We denote with the letter N the refractive index, and we assume that the optical element is surrounded by air, an d that it has a physical thickness t.

A similar interpretation can be applied to other narrow slits that follow other curves in the Fraunhofer domain, namely

$$P(\mu,\zeta) = Q(\mu)\delta\left[\zeta - \sigma\left\lvert\frac{\mu}{\Omega}\right\rvert^m\right]. \tag{8.14}$$

In Eq. (8.14) the Latin letter m is a real number that the indicates power of the monomial μ/Ω. At the output plane of the coherent optical processor, in Fig. 8.3, the complex amplitude distribution displays the changes of the coherent impulse response in terms of the position variable x, as well as in terms of the dimensionless variable z, which represents the variations of optical path difference caused by a refractive optical element; as is indicated in Eq. (8.13).

In Table 8.1 we summarize other possible options when selecting the curve that the narrow slit must follow in the Fraunhofer domain. It is to be noted by using this procedure one can visualize the impact of optical path difference on the behavior of the impulse response for rather unconventional phase delays; as indicated in Fig. 8.5. From this latter figure, it is apparent the unique behavior of the phase mask with fractional power phase profile. Otherwise, we note that the selected phase masks generate asymmetric irradiance distributions, which spread out as the optical path difference increases.

In Fig. 8.6, we show the schematics of an anamorphic optical processor. Now, for the new optical processor, the input is the irradiance distribution that is obtained at the output plane of the previous optical processor. As is apparent from the schematic

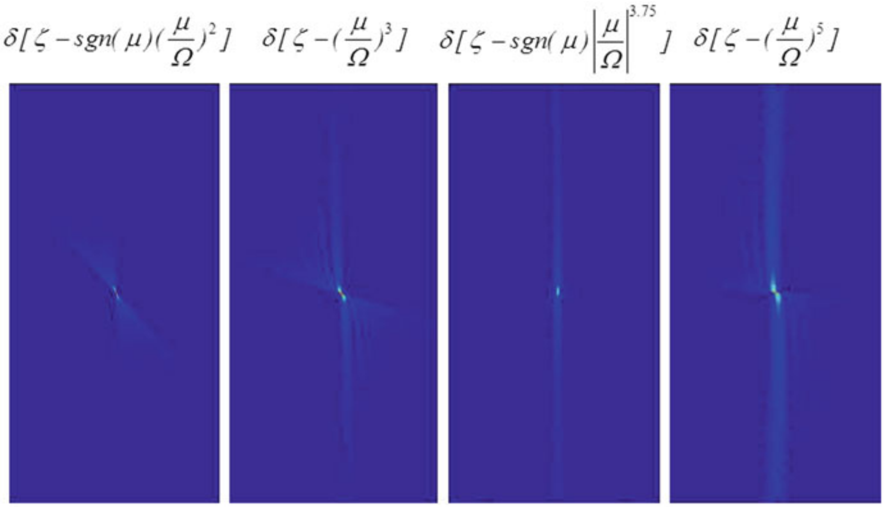

Fig. 8.5 Impulse response as a function of the position and of the optical path difference of several nonconventional optical elements

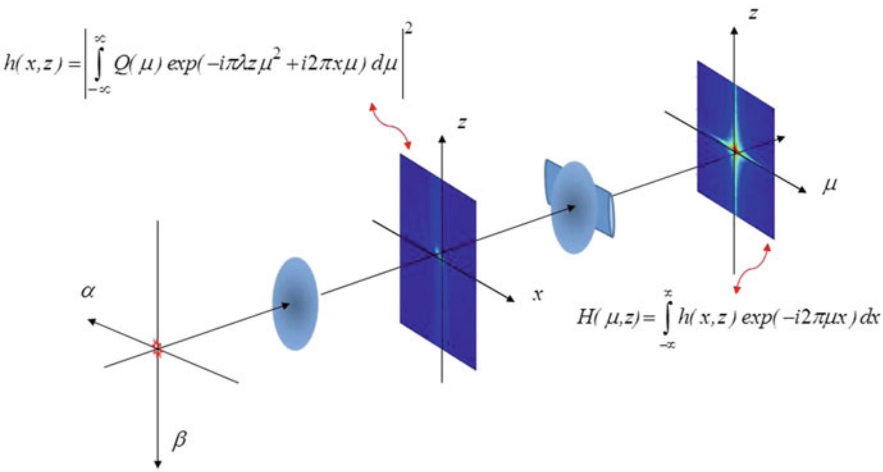

Fig. 8.6 Anamorphic optical processor for displaying (as irradiance variations) the OTF's of several optical elements

diagram in Fig. 8.6, the new anamorphic optical processor implements an imaging operation, with magnification equals to unity, along the vertical axis while it implements a Fourier transformation along the horizontal axis. That is, at the output plane of the new optical processor, the complex amplitude distribution is

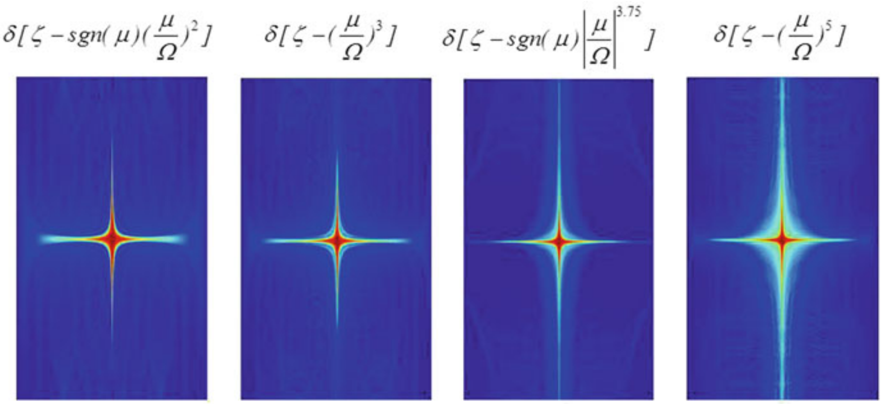

Fig. 8.7 Variations of the MTF as a function of the spatial frequency μ (*horizontal* axis) as well as a function of the optical path difference (*vertical* axis) for four different phase profiles

$$\begin{aligned} H(\mu, z) &= \int_{-\infty}^{\infty}\int_{-\infty}^{\infty} \left|p(x, z')\right|^2 exp(-i2\pi\mu x)\delta(z - z')dxdz' \\ &= \int_{-\infty}^{\infty} |p(x, z)|^2 exp(-i2\pi\mu x)dx. \end{aligned} \tag{8.15}$$

The result in Eq. (8.15) indicates the following. At the output plane of the anamorphic optical processor in Fig. 8.6, one can obtain optically a complex amplitude distribution that is proportional to the Optical Transfer Function (OTF) as a function of both the spatial frequency μ and the axial distance z.

Of course, when visualizing the OTF one uses a square law detector for obtaining the square modulus of the OTF. Hence, the irradiance distribution at the output is the square value of the Modulation Transfer Function (MTF).

In Fig. 8.7 we show the display of the MTF's that are obtained when using, respectively, the curve $\zeta = \mathrm{sgn}\,(\mu)\,(\mu/\Omega)^2$, as well as the curves that are described along the lines 3, 4 and 5 in Table 8.1. It is apparent from Fig. 8.7 that as the optical path difference increases, the MTF's tend to spread out. However, the MTF's exhibit spurious oscillations. It is clear from Fig. 8.7 that again the phase mask with phase profile with fractional power (m = 3.75) has reduced spurious oscillations. In the following section, while we describe another method for visualizing the impact of focus error on the MTF, we discuss an optical technique that strongly reduces the spurious oscillations on the MTF.

Several years ago, some of us established a link between the OTF suffering from focus errors and the ambiguity function of the pupil aperture [23]. Later on, the ambiguity function was applied as a mathematical tool for proposing optical masks that reduce the impact of focus error on the OTF [35].

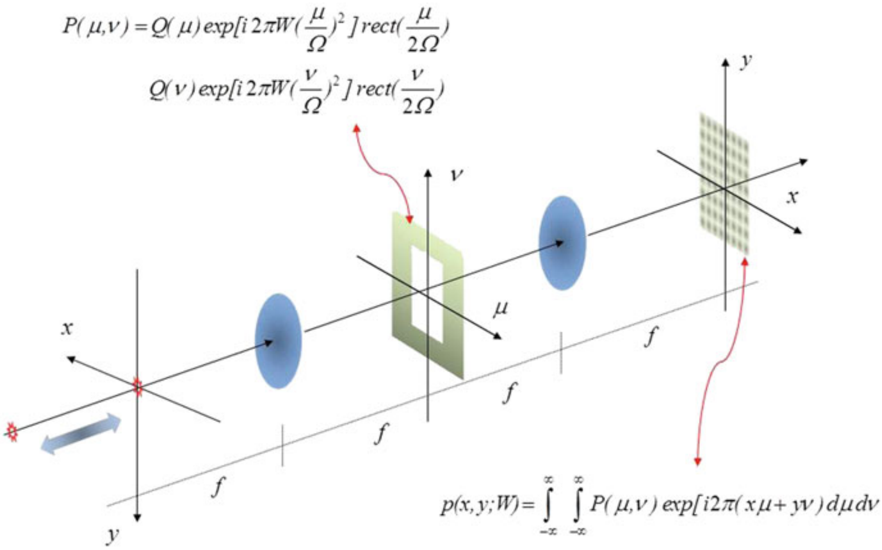

Fig. 8.8 Schematics of an optical processor that is used for analyzing out-of-focus imagery

8.3 Visualizing the MTF with Extended Depth of Field

Here, for the sake of completeness of our presentation, we discuss briefly the out-of-focus image formation process when using a classical optical processor; as is depicted in Fig. 8.8. For further details please see reference [36]. In what follows we consider that the square law is located at fixed position, at the output plane, while the pinhole size source moves along the optical axis of the optical processor. Consequently, the geometrical image of point source is located before or after the detector plane. From the viewpoint of wave aberration, within the paraxial regime, one can represent the location of the point source along the optical axis, by using the following generalized pupil function

$$P(\mu; \mathrm{W}_{2,0}) = Q(\mu) exp \left\{ i2\pi \left(\frac{W_{2,0}}{\lambda} \right) \left(\frac{\mu}{\Omega} \right)^2 \right\}. \tag{8.16}$$

In Eq. (8.16) we denote as $\mathrm{Q}(\mu)$ the complex amplitude transmittance of the pupil mask; and the letter $\mathrm{W}_{2,0}$ denotes the wavefront focus error coefficient. The Greek letter Ω denotes the cut-off spatial frequency of the rectangular pupil aperture.

For simplifying the notation it is convenient to employ the dimensionless parameter

$$W = \frac{W_{2,0}}{\lambda} \tag{8.17}$$

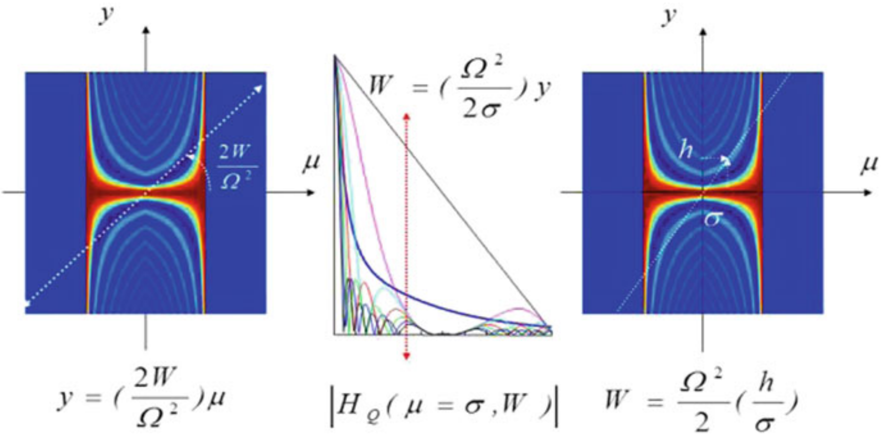

Fig. 8.9 Scanning lines along the ambiguity function for obtaining the values of the out-of-focus MTF

As is well known, the OTF of Eq. (8.16) is

$$H_Q(\mu; W) = N_{orma} \int_{-\infty}^{\infty} P\left(\nu + \frac{\mu}{2}\right) P^*\left(\nu - \frac{\mu}{2}\right) d\nu$$
$$H_Q(\mu; W) = N_{orma} \int_{-\infty}^{\infty} Q\left(\nu + \frac{\mu}{2}\right) Q^*\left(\nu - \frac{\mu}{2}\right) exp\left[i2\pi\left(\frac{2W\mu}{\Omega^2}\right)\nu\right] d\nu. \quad (8.18)$$

In Eq. (8.18) the upper case letter N_{orma} denotes a suitable normalization factor. On the other hand, the ambiguity function of the pupil mask, Q(μ), is

$$A_Q(\mu, y) = N_{orma} \int_{-\infty}^{\infty} Q\left(\nu + \frac{\mu}{2}\right) Q^*\left(\nu - \frac{\mu}{2}\right) exp\left[i2\pi y\nu\right] d\nu. \quad (8.19)$$

From a simple comparison between Eqs. (8.18) and (8.19), we note that

$$y = \left(\frac{2W}{\Omega^2}\right) \mu. \quad (8.20)$$

If in the display of the ambiguity function (as that at the left hand-side of Fig. 8.9) one traces a straight-line, crossing the origin; the slope is proportional to the amount of focus error; as indicated in Eq. (8.20). If one selects a value of the spatial frequency, say $\mu = \sigma$, then the variations of the OTF for variable focus errors can be visualized by moving up or down along a vertical line; as depicted at the centre of Fig. 8.9. Furthermore, for a given position along the vertical line, say $y = h$, the focus error coefficient is $W = (\Omega^2/2)\ (h/\sigma)$.

Next, we recognize that for displaying the ambiguity function, one can use the anamorphic processor in Fig. 8.10. See for example reference [36]. In Fig. 8.10, we

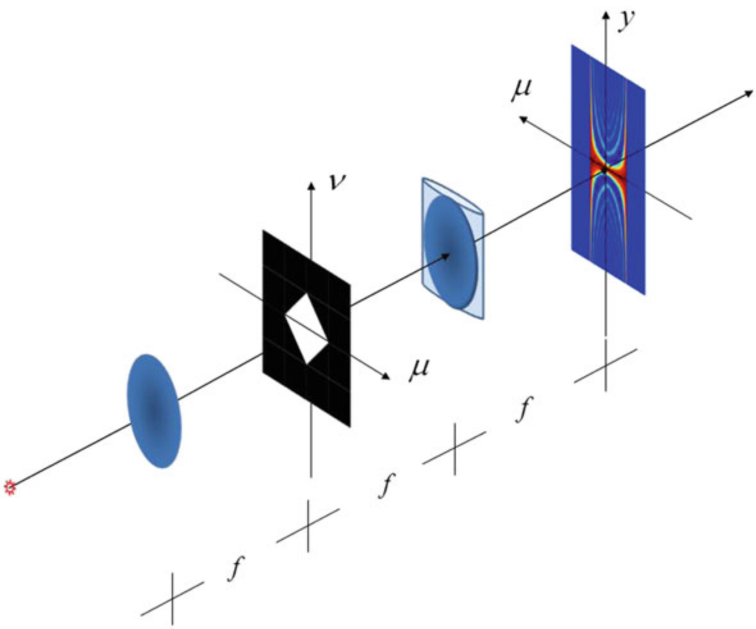

Fig. 8.10 Anamorphic optical processor that is used for visualizing the Ambiguity function

indicate that the input for the anamorphic processor is the *Product Spectrum*, which is

$$P_Q(\mu,\nu) = Q\left(\nu + \frac{\mu}{2}\right) Q^*\left(\nu - \frac{\mu}{2}\right). \tag{8.21}$$

For a clear pupil aperture, $Q(\mu) = \mathrm{rect}(\mu/2\Omega)$ then the Product Spectrum is

$$P(\mu,\nu) = rect\left(\frac{\mu}{4\Omega}\right) rect\left(\frac{\nu}{2\Omega - |\mu|}\right). \tag{8.22}$$

We note that the anamorphic processor, in Fig. 8.10, performs an imaging operation, with unit magnification, along the horizontal axis. From Fig. 8.10 and Eq. (8.22) the following considerations are apparent. Inside the passband, $|\mu| \le 2\Omega$, a vertical line along the product spectrum is bounded by the function *rect* $[\nu/\,(2\Omega - |\mu|)]$.

Hence, at the output plane of the optical processor, along the vertical axis one has the Fraunhofer diffraction pattern of a rectangular window. Thus, at the output plane of the optical processor, the complex amplitude distribution is

$$A_Q(\mu, y) = \left(1 - \frac{|\mu|}{2\Omega}\right) \sin c\left[\left(1 - \frac{|\mu|}{2\Omega}\right) y\right] \tag{8.23}$$

In other words, the ambiguity function is composed by a series of sinc functions with variable half-width. Consequently, the out-of-focus OTF exhibits a large number of

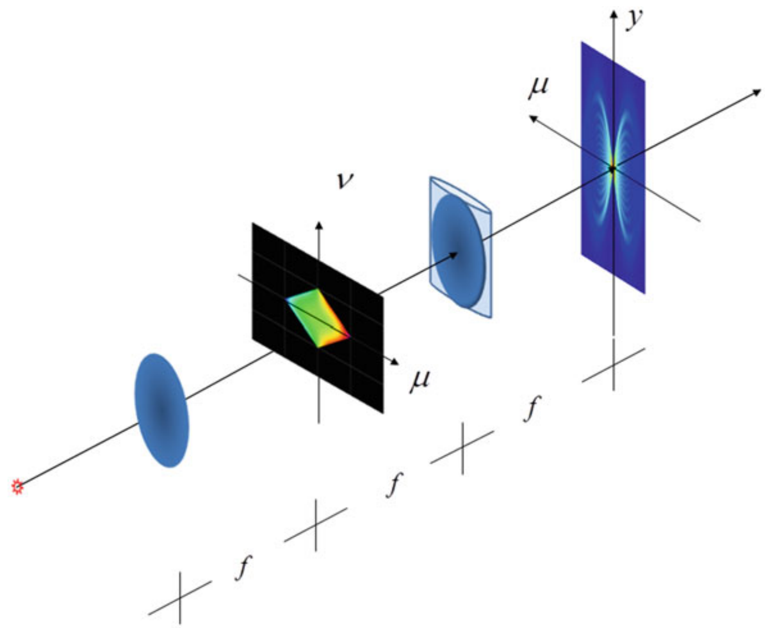

Fig. 8.11 Use of phase-only masks for obtaining ambiguity functions with "Bow-Tie" effect

zero crossings. If one wants to modify this result, then one needs to consider another possible ambiguity functions. For example, if at the ***Product spectrum*** we have a vertical line that has a quadratic phase factor,

$$P(\mu, \nu) = exp\left[i2\pi a(\frac{\nu}{\Omega})^2\right] rect\left[\frac{\nu}{2\Omega - |\mu|}\right] rect\left[\frac{\mu}{4\Omega}\right]. \tag{8.24}$$

For obtaining this type of ***Product Spectrum***, one needs a cubic phase mask, as proposed by Dowski and Cathey. If, as depicted in Fig. 8.11, now we take the complex amplitude transmittance along a vertical line vertical axis, and we evaluate the Fourier transform of Eq. (8.24), we obtain

$$\begin{aligned} A_Q(\mu, y) = rect\left(\frac{\mu}{4\Omega}\right) \\ \int_{-\frac{(2\Omega-|\mu|)}{2}}^{\frac{(2\Omega-|\mu|)}{2}} exp\left\{i2\pi\left[a\left(\frac{\mu}{\Omega}\right)^2 + y\nu\right]\right\} d\nu. \end{aligned} \tag{8.25}$$

It is apparent from Eq. (8.25) that along the y-axis, the ambiguity function results from the lateral superposition of Fresnel diffraction patterns of rectangular windows, which have variable width. See Fig. 8.11.

Since any vertical line is a Fresnel diffraction pattern, then the ambiguity function spreads all over the (μ, y) plane. This behaviour is known as the "bow-tie effect".

See reference [37]. As a consequence, the OTF's have low sensitivity to focus errors. Of course, one can extrapolate this previous result, by exploring the use of high order aberration polynomials. That is,

$$Q(\mu) = exp\left\{i2\pi a\left(\frac{\mu}{\Omega}\right)^{2m+1}\right\} rect\left(\frac{\mu}{2\Omega}\right). \tag{8.26}$$

One can guess that the phase mask described in Eq. (8.26) will be able to spread the ambiguity function along the vertical axis; as is depicted in Fig. 8.11. Consequently, one expects that this type of masks will be able to extend the depth of field. However, it is relevant to note that these types of high order phase masks (including the cubic phase mask) introduce spurious oscillations. For reducing this undesirable feature, one can use a Gaussian apodizer on the pupil aperture; as part of the spatial filter. In other words, now the complex amplitude transmittance of the pupil aperture is

$$Q(\mu) = \exp\left\{i2\pi a\left(\frac{\mu}{\Omega}\right)^{2m+1} - c\left(\frac{\mu}{\Omega}\right)^{2}\right\} \mathrm{rect}\left(\frac{\mu}{2\Omega}\right). \tag{8.27}$$

In Eq. (8.27) the lower case letter "c" denotes a damping factor, in the amplitude variations, which are described by a Gaussian profile. See reference [38].

At the top of Fig. 8.12, we show the MTF of a cubic phase mask for $W = 0$ and for $W = 3$. One can note that there are spurious oscillations. At the bottom of Fig. 8.12, we show the MTF that is obtained if one use the complex amplitude transmittance in Eq. (8.27) for $m = 1$. From the results at the bottom of Fig. 8.12, it is apparent that a Gaussian apodizer is able to reduce unwanted oscillations in the MTF; without spoiling the low sensitivity of the MTF to focus errors.

The tapering mask with Gaussian profile has the following additional advantages, which are illustrated in Fig. 8.13. First, by using a Gaussian apodizer the 2-D rectangular pupil aperture is transformed into a nearly circularly symmetric aperture; as is indicated along the first column of Fig. 8.13.

Furthermore, the Gaussian apodizer reduces the diffraction lobes in the asymmetric PSF; as depicted along the second column of Fig. 8.13. We note also that the Gaussian apodizer broadens the MTF, as shown along the third column of Fig. 8.13. The above results can also be visualized in terms of the product spectrum and the ambiguity function; as we depict next.

Along the first column in Fig. 8.14, we show the influence that a Gaussian mask has on the product spectrum. Along the second column, first line, in Fig. 8.14 we display zero-phase variations inside the support of the product spectrum. Along the second column, line two, of Fig. 8.14 we show as colour variations the profile of a 2-D cubic phase mask. And along the second column, line three, in Fig. 8.14 we show the phase delays of a 2-D cubic phase mask.

From the third column in Fig. 8.14 the following characteristics are apparent. Along the first line and third column of Fig. 8.14, we have that the modulus of the ambiguity function has several regions with zero values. Then as depicted in the second line and third column of Fig. 8.14, if one uses a cubic phase masks the modulus of the ambiguity function has extended regions with nonzero values. However, the

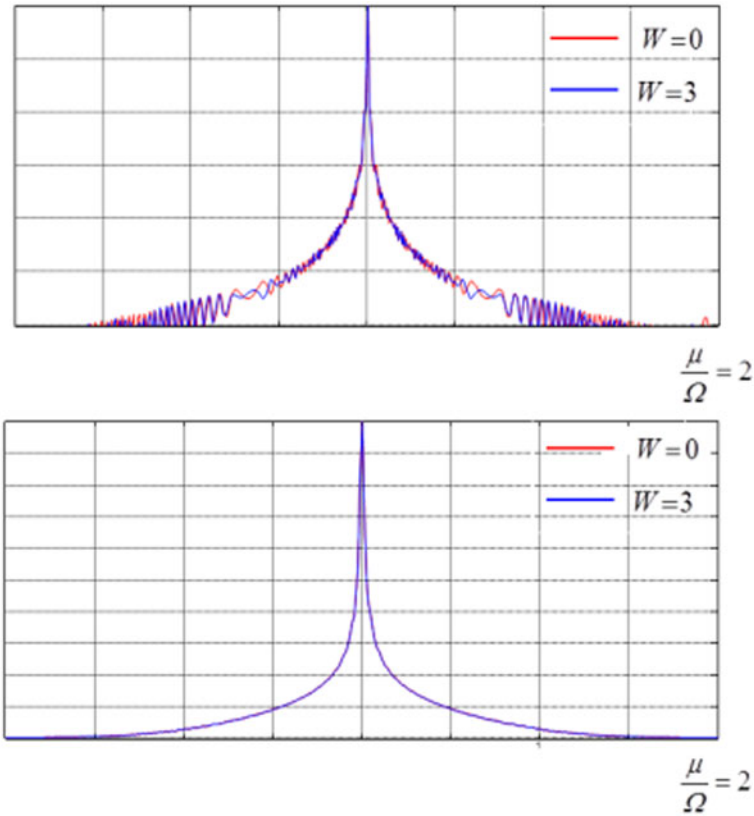

Fig. 8.12 Use of a Gaussian mask for reducing the spurious oscillations on the in-focus MTF and out-of-focus MTF

nonzero values have spurious oscillations. Finally, as shown in the second line and third column of Fig. 8.14, if one uses a Gaussian mask together with a cubic phase masks one can reduce the spurious oscillations on the regions with nonzero values.

For obtaining the numerical simulations in Fig. 8.14, which are described by Eq. (8.27), we select the values $a = 33$, $n = 1$ and $c = 0.44$. These results are generalized in reference [39], where we use the following definition for hyper Gaussian masks. In what follows we consider that the complex amplitude transmittance of the pupil aperture is

$$Q(\mu) = exp\left\{ i2\pi\, sgn\,(\mu) \left| \frac{\mu}{\Omega} \right|^m \right\} \\ exp\left\{ -c \left| \frac{\mu}{\Omega} \right|^n \right\} rect\left(\frac{\mu}{2\Omega} \right) \tag{8.28}$$

In Eq. (8.28) the letters m and n denote real positive numbers. Since the values of m are no longer integer numbers, then the first term in Eq. (8.28) represents a fractional

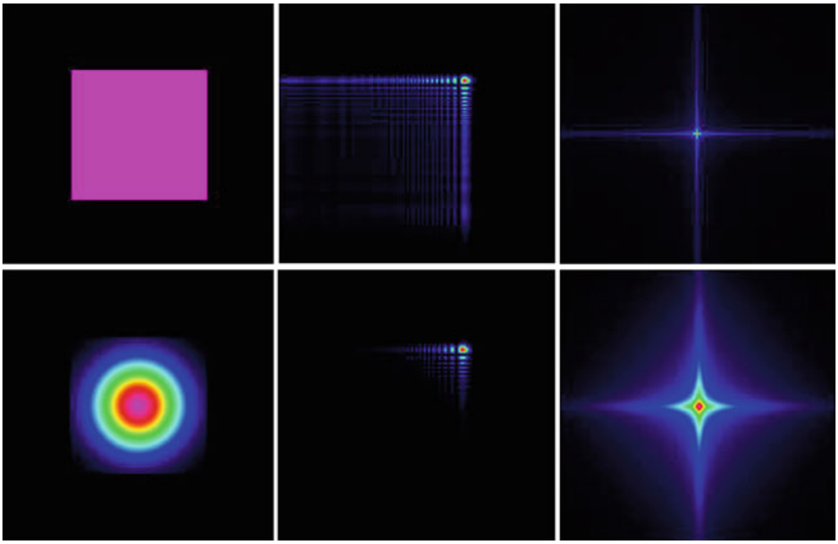

Fig. 8.13 Influence of Gaussian tapering on the pupil aperture, the PSF and the MTF

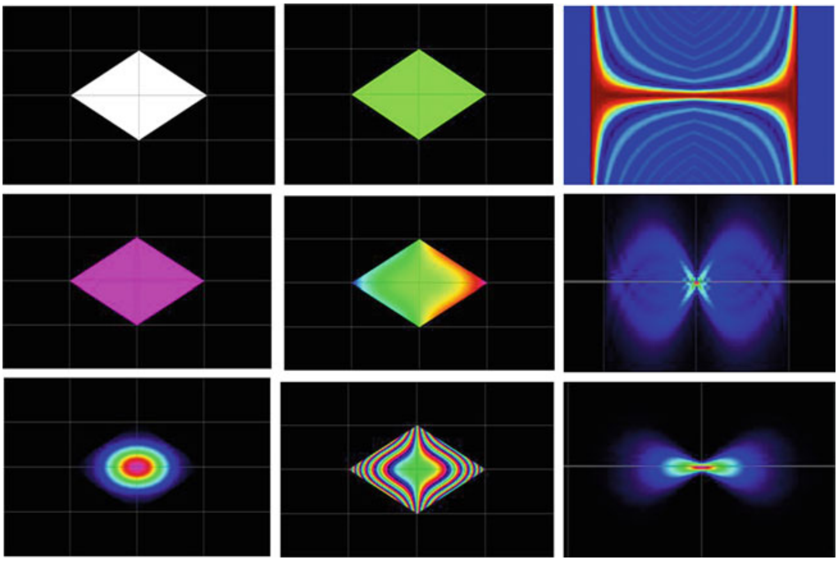

Fig. 8.14 The impact of a Gaussian apodizer on product spectrum, and the resultant ambiguity function

order wavefront. Due to the factor sgn(μ), denoting the signum function, the wavefront has phase delays that are odd functions. Furthermore, regarding the second term in Eq. (8.28), for values of n such that $n < 2$ the amplitude transmittance is denoted as sub Gaussian function; for $n = 2$, the amplitude transmittance is represented by a

Gaussian function; while for $n > 2$, the amplitude transmittance is denoted as super Gaussian function. We employ the generic word hyper Gaussian for encompassing the cases under exploration with $0 < n < 10$.

For our numerical simulations we use the following definitions that apply for the 1-D case. For variable values of focus error, the normalized irradiance distribution of the impulse response is

$$|q(x;W)|^2 = \left| \int_{-\infty}^{\infty} Q(\mu) exp\left[i2\pi \left(W\left(\frac{\mu}{\Omega}\right)^2 + x\mu \right) \right] rect\left(\frac{\mu}{2\Omega}\right) d\mu \right|^2. \quad (8.29)$$

And of course, the MTF is

$$|H(\mu;W)| = \int_{-\infty}^{\infty} |q(x;W)|^2 exp(-i2\pi\mu x) dx. \quad (8.30)$$

We evaluate numerically Eqs. (8.29) and (8.30) using the fast Fourier transform (FFT) algorithm described in reference [40]. We use 1024 points and a set of Graphic User Interface (GUI) elements. The numerical process is written in C++ language. Our numerical search starts by considering the values that were identified in the previous section. Then, we modify the parameters "a" and "c" in Eq. (8.28) until the variations of the MTF have a mean square error that is less than 10^{-4}.

Once that the 1-D sub Gaussian masks were identified, Q(μ) in Eq. (8.28), the complex amplitude transmittance of the 2-D masks are obtained as the product Q(μ) Q(ν). After extensive numerical evaluations, we identify the following interesting result.

Inside the range $0 \leq W \leq 3$, one can obtain a MTF that varies slowly with focus error, by using a fractional wavefront $m = 2.75$ that has a maximum optical path difference value $a = 27$, together with a sub Gaussian mask $n = 1.75$ and attenuation factor $c = 1.61$.

In Fig. 8.15, along the second column, we plot the 1-D profiles. And along the third column, we show the following 2-D displays. In the first line, we place a pseudo color picture of the 2-D amplitude transmittance variations. In the second line, we place an interferogram of the 2-D phase variations. In the third line and the fourth line, we use pseudo color pictures for displaying the 2-D variations of the PSF and the MTF, respectively.

Finally, we note that these optical characteristics preserve the resolution associated with a full aperture. However, these results come at the expense of reducing the light gathering power by a factor slightly greater than two.

8.4 Tunable Devices for Extending the Depth of Field

According to Plummer, Baker and van Tassel [41], Kitajima was the first person that proposed to implement suggested variable optical power lenses, by using a pair of cubic phase masks [42]. Years later, Lohmann [43–45] and Alvarez [46, 47] re-discovered independently and simultaneously Kitajima's technique .

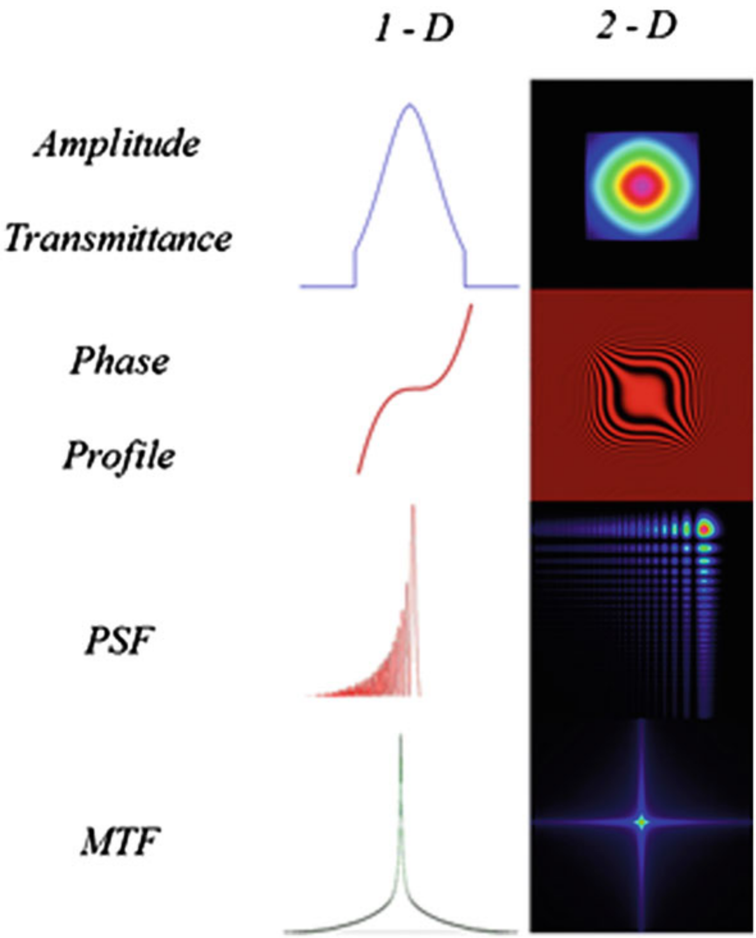

Fig. 8.15 Resultant PSF and resultant MTF associated to the hyper Gaussian apodizer in Eq. (8.28)

In what follows, our aim is threefold. First, we indicate that Kitajima's technique, commonly known as Alvarez-Lohmann lenses, is also useful for implementing tunable absorption masks, which are useful for setting hyper Gaussian apodizers with tunable half-width. Second, we show that by using two suitable helical refractive elements, one can control the optical path difference of radial focalizers. And third, we discuss the use of a pair of helical distributed amplitude masks for tuning the damping coefficient of Gaussian-like windows.

For achieving our first goal, we note that Alvarez and Lohmann lenses employ two phase masks that form a pair. The amplitude transmittance of a single mask is the complex conjugate of the other mask. Then, by introducing a lateral displacement between the two masks, say by the spatial frequency σ, one sets a varifocal lens. In mathematical terms, for the 1-D case, a single element of the pair has the following complex amplitude transmittance

$$Q(\nu) = exp\left\{i2\pi a\left(\frac{\nu}{\Omega}\right)^3\right\}. \tag{8.31}$$

In Eq. (8.31) the lower case letter "a" denotes the optical path difference in units of the wavelength λ. Next, it is convenient to use two elements. Each element has the complex amplitude transmittance in Eq. (8.31). However when setting the pair, one element is the complex conjugate of the other. Then, one introduces a lateral displacement between the elements of the pair. In this manner, the overall complex amplitude transmittance is

$$\begin{aligned} P_Q(\nu;\sigma) &= Q\left(\nu + \frac{\sigma}{2}\right) Q^*\left(\nu - \frac{\sigma}{2}\right) \\ &= exp\left\{i\left(\frac{a\pi}{2}\right)\left(\frac{\sigma}{\Omega}\right)^3 + i2\pi\left(\frac{a\sigma}{\Omega}\right)\left(\frac{\nu}{\Omega}\right)^2\right\}. \end{aligned} \tag{8.32}$$

In Eq. (8.32) the quadratic variation, in the variable ν, is similar to the amplitude transmittance of a lens. However, it is important to recognize that by changing σ, one can tune the power of a lens.

Moreover, we recognize that the physical procedure for obtaining the result in Eq. (8.32) is similar to the mathematical operation that is involved when evaluating the OTF in Eq. (8.18). Hence, we claim the following.

By visualizing the amplitude PSF of the pair in Eq. (8.32), one visualizes the ambiguity function of a single element of the pair, as in Eq. (8.18). That is,

$$p_Q(x;\sigma) = N_{orma}\int_{-\infty}^{\infty} P_Q(\nu,\sigma) exp\left[i2\pi x\nu\right] d\nu = A_Q(\sigma, x). \tag{8.33}$$

Now, we have a physical method (the use of a pair of phase masks) for understanding the influence that a single element has on the behavior of the ambiguity function.

Furthermore, one can propose the use of a mask that has phase variations to the four-power for implementing a cubic phase mask, with controllable optical path difference.

For this application, we consider that the complex amplitude transmittance of a single element is

$$Q(\nu) = exp\left\{i2\pi a\left[\left(\frac{\nu}{\Omega}\right)^4 - \frac{1}{2}\left(\frac{\nu}{\Omega}\right)^2\right]\right\}. \tag{8.34}$$

As before, we employ a phase conjugated pair and we introduce a lateral displacement between the members of the pair. Then, we generate the following generalized pupil function

$$\begin{aligned} P_Q(\nu;\sigma) &= Q\left(\nu + \frac{\sigma}{2}\right) Q^*\left(\nu - \frac{\sigma}{2}\right) \\ &= exp\left\{i2\pi\left(\frac{4a\sigma}{\Omega}\right)\left(\frac{\nu}{\Omega}\right)^3\right\} \\ &\quad exp\left\{i2\pi\left(\frac{a\sigma}{\Omega}\right)\left[\left(\frac{\sigma}{\Omega}\right)^2 - 1\right]\left(\frac{\nu}{\Omega}\right)\right\}. \end{aligned} \tag{8.35}$$

From Eq. (8.35) one notes that by changing the value of σ, one can change the optical path difference of a cubic phase mask. In other words, we can implement a varicubic phase masks. However, the proposed phase mask generates also a linear phase variation. The influence of this unwanted term can be reduced by properly selecting the values of the initial optical path difference and the maximum value of the lateral displacement. See for example [48–50].

For achieving our second goal, in this section, we describe the use of a pair of amplitude masks that help for setting a Gaussian spatial filter, with adjustable half-width [50]. We start our discussion, by considering the amplitude transmittance of the first amplitude element of the proposed pair

$$T_1(\mu) = exp\left\{-c\left[1+\left(\frac{\mu}{\Omega}\right)^3\right]\right\} rect\left(\frac{\mu}{4\Omega}\right). \tag{8.36}$$

As before, in Eq. (8.36) we use a lower case letter "c" for denoting a dimensionless damping factor of the Gaussian function. From Eq. (8.36), we note that the length of the mask is 4Ω. At its edges the amplitude transmittance has real positive values. Now, the amplitude transmittance of the of the second mask is

$$T_2(\mu) = exp\left\{-c\left[1-\left(\frac{\mu}{\Omega}\right)^3\right]\right\} rect\left(\frac{\mu}{4\Omega}\right). \tag{8.37}$$

Again the length of the mask is 4Ω, and at its edges the amplitude transmittance has real positive values. By introducing a lateral displacement, σ; between the masks, the overall amplitude transmittance inside the pupil aperture is

$$T(\mu;\sigma) = T_1\left(\mu+\frac{\sigma}{2}\right) T_2\left(\mu-\frac{\sigma}{2}\right). \tag{8.38}$$

If one substitutes Eqs. (8.36) and (8.37) in Eq. (8.38) one obtains

$$\begin{aligned} T(\mu;\sigma) = exp&\left\{-2c\left[1+\left(\frac{\sigma}{2\Omega}\right)^3\right]\right\} \\ &exp\left\{-\left(\frac{3c\sigma}{4\Omega}\right)\left(\frac{\mu}{\Omega}\right)^2\right\} rect\left(\frac{\mu}{2\Omega}\right). \end{aligned} \tag{8.39}$$

It is apparent from Eq. (8.39) that inside the pupil aperture, the overall amplitude transmittance varies as a Gaussian function. Its half-width can be modified by changing the lateral amount of displacement in the Fourier domain. In reference [51] we have extended the above result to 2-D.

Here it is relevant to note that if one uses simultaneously the tunable cubic phase mask and the tunable Gaussian amplitude mask, then one has two extra degrees of freedom for setting the pre-processing filter; as was discussed in the previous section. However, we also note that so far our tunable devices are only useful when the complex amplitude profiles can be expressed as monomials to an integer power. We discuss next an optical technique for overcoming this limitation.

After proposing his varifocal technique, Lohmann applied his result for generating tunable zone plates. Lohmann and Paris have proposed the use of helical modulations [52] for generating other types of varifocal zone plates. In their proposal, Lohmann and Paris suggested the use of an average angular operation for achieving tunable devices that have only radial variations.

Later on, Burch and Williams [53] used Lohmann's technique for implementing an alignment device, which has the interesting twist of incorporating and additional phase factor as proposed for Alvarez in his varifocal technique.

Bernet and coworkers have revisited the use of ***diffractive elements*** for implementing varifocal lenses using helical variations [54–56]. And rather recently, some of us, have suggested the use of two helical ***refractive elements*** for setting several varifocal devices [57, 58]. In what follows we revisited these latter proposals.

For achieving our final goal, in this section, we note that Bryngdahl analysed interferograms in terms of polar coordinates [59]. In Fig. 8.16 we show some schematic diagrams for describing the generation of interference patterns. The interferograms are generated by superimposing a plane reference wavefront with one of the following object beams. At the top of Fig. 8.16 the object beam has quadratic radial variations; while at the middle of Fig. 8.16 the object beam has linear helical variations (angular variations). At the bottom of Fig. 8.16 the object beam has both radial as well as helical variations.

For describing the optical devices of our interest, we consider the following complex amplitude transmittance

$$Q(\rho, \varphi) = exp\{iaR(\rho)\varphi\}. \tag{8.40}$$

In Eq. (8.40) we use the Greek letters ρ and φ for denoting the radial spatial frequency and the polar angle at the pupil aperture, respectively. The Latin letter a represents the optical path difference of the optical device. For making comparisons it is useful to remember that a lens, with fixed optical power, has the following complex amplitude transmittance

$$Q(\rho, \varphi) = exp\left\{ia\left(\frac{\rho}{\Omega}\right)^2\right\}. \tag{8.41}$$

In Eq. (8.41) the Greek letter Ω denotes the maximum value of the radial spatial frequency. This value is typically called the cut-off spatial frequency of the pupil aperture. The interferogram of the quadratic phase variation in Eq. (8.41) is a Fresnel zone plate; as is shown in the left-hand side of Fig. 8.17.

If the lens has also helical variations then the complex amplitude transmittance is

$$Q(\rho, \varphi) = exp\left\{ia\left(\frac{\rho}{\Omega}\right)^2\varphi\right\}. \tag{8.42}$$

At the right hand side of Fig. 8.17, we show the interference pattern that is generated between a plane wavefront and the complex amplitude transmittance in Eq. (8.42). At the left-hand side of Fig. 8.18, we show the phase variations in Eq. (8.42).

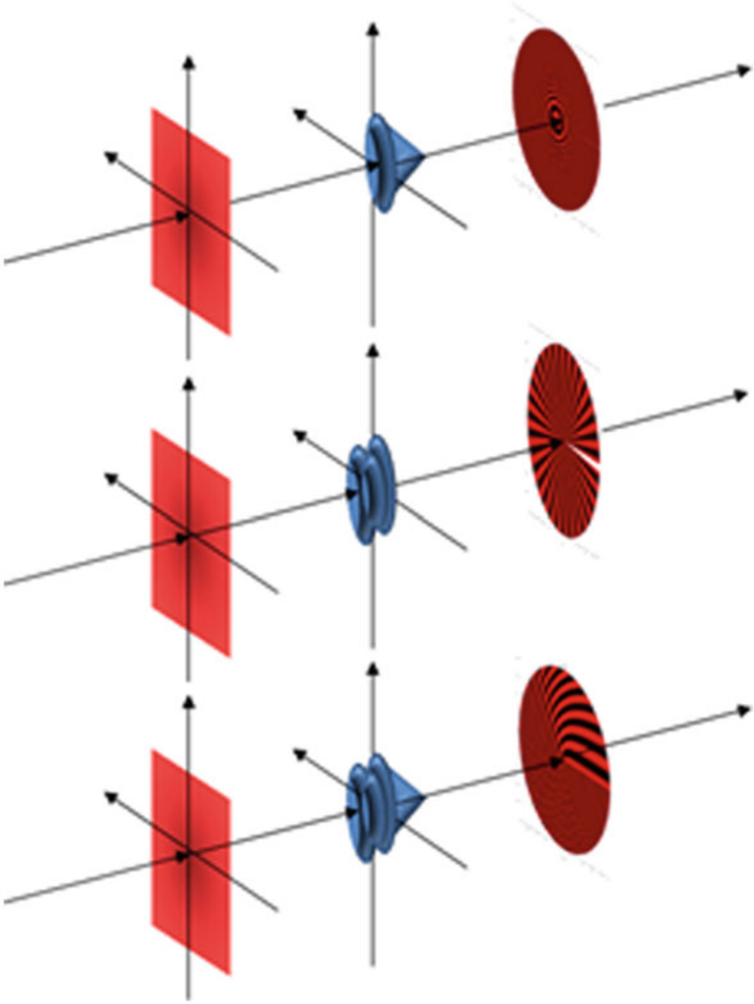

Fig. 8.16 Interferograms obtained as the interference between a reference plane wavefront and three different object beams: **a** radial beam, **b** helical beam, and **c** a beam having both radial and helical variations. The object beam is obtained after passing through the optical device

The interferogram, at the right-hand side of the same figure, was first discussed by Lohmann and Paris.

Next, we note that rather than introducing a lateral displacement between the elements of the pair (as depicted in at the left-hand side of Fig. 8.19) we can introduce an in-plane rotation between the elements of the pair (as depicted at the right-hand side of Fig. 8.19).

Fig. 8.17 Interference patterns that are obtained using a reference plane wavefront and three different object beams: radial beam, helical beam, and a beam having both radial and helical variations, respectively

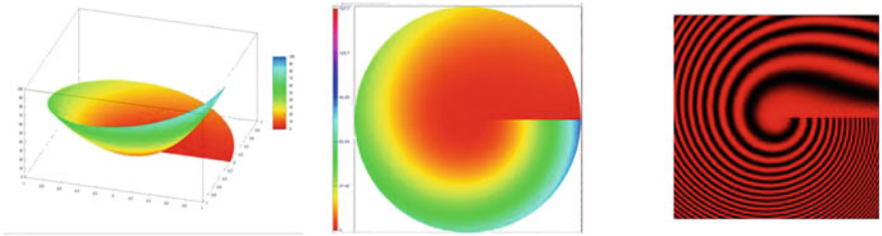

Fig. 8.18 Three different views of the helical phase in Eq. (8.41): 3-D curve, 2-D pseudo color variations and the interference pattern that is generated when using as reference beam a uniform plane wave

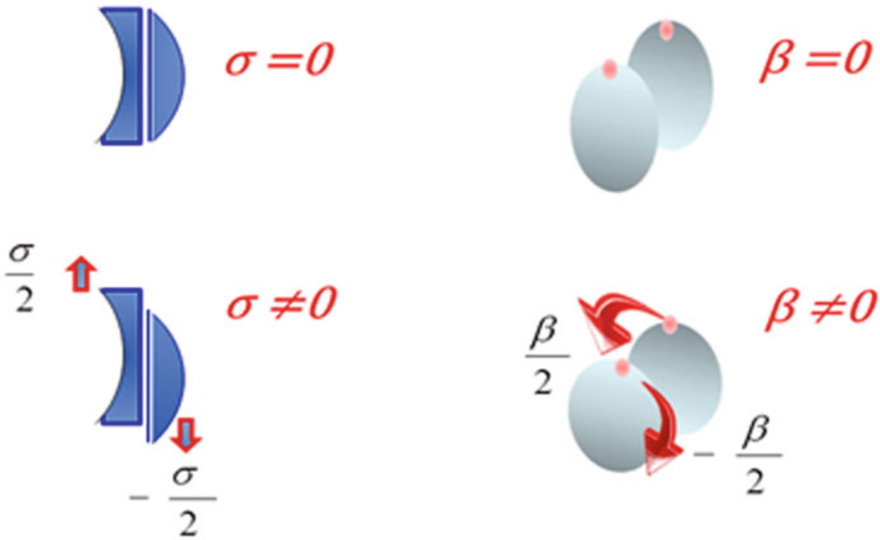

Fig. 8.19 Tunable devices using a controllable lateral shear, with spatial frequency σ, or a controllable in-plane rotation angle β

For this later application, we consider that the complex amplitude transmittance of the first refractive element is

$$T_1(\rho,\varphi) = exp\left\{i2\pi a\varphi\left(\frac{\rho}{\Omega}\right)^m\right\}. \tag{8.43}$$

In Eq. (8.42) the Latin letter m denotes the power of the radial variable. The complex amplitude transmittance of the second refractive element is the complex conjugate of the first element. That is,

$$T_2(\rho,\varphi) = exp\left\{-i2\pi a\varphi\left(\frac{\rho}{\Omega}\right)^m\right\}. \tag{8.44}$$

Now, if both refractive elements are used as a pair, and we introduce an in-plane rotation between the elements of the pair (say by an angle β) the overall complex amplitude transmittance is

$$\begin{aligned} T(\rho;\beta) &= T_1\left(\rho,\varphi+\frac{\beta}{2}\right)T_2\left(\rho,\varphi-\frac{\beta}{2}\right) \\ &= exp\left\{i2\pi a\beta\left(\frac{\rho}{\Omega}\right)^m\right\}. \end{aligned} \tag{8.45}$$

It is apparent from Eq. (8.44) that the complex amplitude transmittance of the pair is independent of the helical variable φ. Furthermore, we recognize that the angle β modifies linearly the value of the optical path difference. And in this manner, one can exploit the angular variation for controlling the optical path difference of the radial focalizer.

In Fig. 8.20, we show the use of the tunable focalizer as spatial filters in an afocal, optical processor. It is convenient to note that the proposed optical technique, as expressed in Eq. (8.44), can be extended to wide range of radial variations. In mathematical terms,

$$\begin{aligned} T(\rho;\beta) = exp&\left\{i2\pi a\left(\varphi+\frac{\beta}{2}\right)R(\rho)\right\} \\ exp&\left\{-i2\pi a\left(\varphi-\frac{\beta}{2}\right)R(\rho)\right\} \\ &= exp\{i2\pi a\beta R(\rho)\}. \end{aligned} \tag{8.46}$$

Next we describe a method for optically tuning the half-width of hyper Gaussian apodizers; as is discussed in references [60, 61]. As depicted in Fig. 8.20, we consider that at the Fraunhofer plane we place two amplitude masks forming a pair. The amplitude transmittance of the first mask is

$$T_1(\rho,\varphi;n) = exp\left\{-\frac{1}{2}\left(\frac{\rho}{\Omega}\right)^n\left(1+\frac{\varphi}{2\pi}\right)\right\}circ\left(\frac{\rho}{\Omega}\right). \tag{8.47}$$

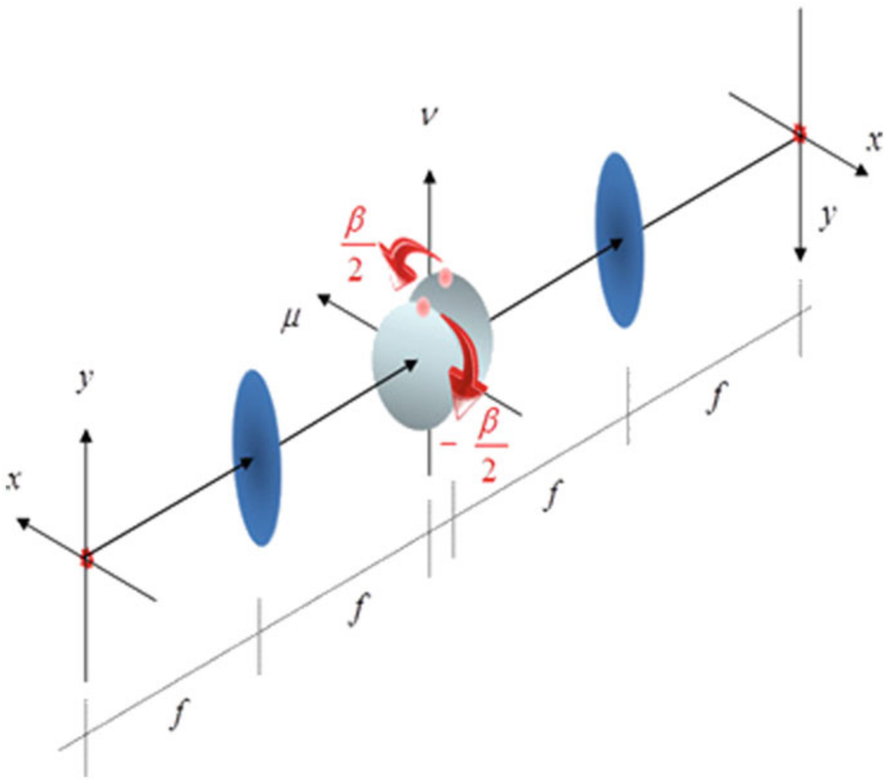

Fig. 8.20 Optical processor that employs a pair of helical masks at the Fraunhofer plane

In Eq. (8.47) the Greek letters ρ and φ denote again the polar coordinates in the pupil aperture. The maximum value of the polar coordinate, ρ, is the cut-off spatial frequency Ω. The circ function represents the pupil aperture, $0 \leq \rho \leq \Omega$. The Latin letter "n" denotes the power of the radial variable. The polar angle varies inside the interval $0 \leq \varphi < 2\pi$. We note that if $n = 2$, one has an amplitude transmittance that is proportional to a Gaussian function. A sub Gaussian mask is defined by a value of $n < 2$. And again if $n > 2$, one has super Gaussian masks. We denote as hyper Gaussian any amplitude transmittance within the range $0 < n < 10$. We recognize that the amplitude transmittance in Eq. (8.47) is bounded.

The amplitude transmittance of the second mask is

$$T_2(\rho, \varphi; n) = exp\left\{-\frac{1}{2}\left(\frac{\rho}{\Omega}\right)^n\left(1 - \frac{\varphi}{2\pi}\right)\right\} circ\left(\frac{\rho}{\Omega}\right). \tag{8.48}$$

Again we note that the amplitude transmittance in Eq. (8.48) is bounded. Next, we place in contact these two previously described masks for setting a pair. The overall complex amplitude transmittance becomes

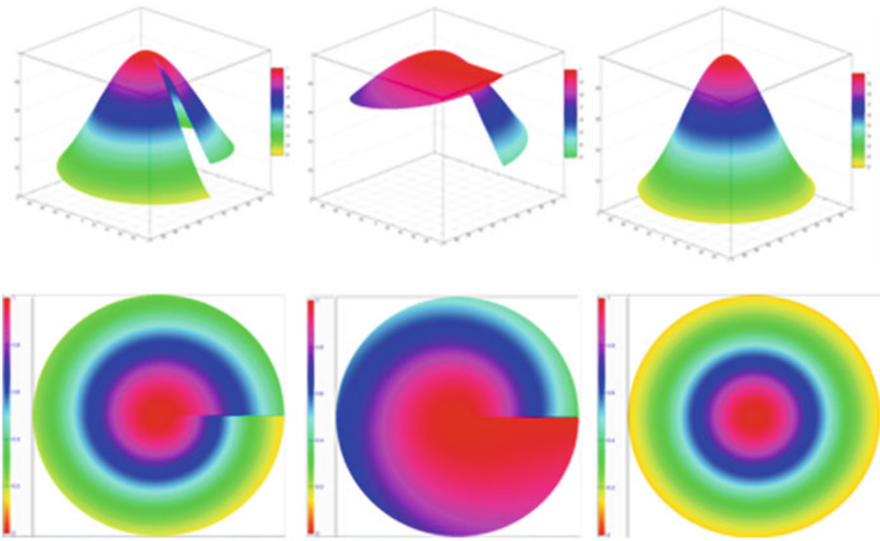

Fig. 8.21 Tuning the half-width of a Gaussian apodizer by the use of a pair of asymmetric masks that have helical amplitude variations

$$\begin{aligned} T(\rho;\beta) &= T_1\left(\rho,\varphi+\frac{\beta}{2}\right) T_2\left(\rho,\varphi-\frac{\beta}{2}\right) \\ &= exp\left\{-\frac{\beta}{4\pi}R(\rho)\right\} circ\left(\frac{\rho}{\Omega}\right). \end{aligned} \tag{8.49}$$

From Eq. (8.49) it is clear that the overall amplitude transmittance does not longer depend on the angular variable φ. That is, the overall amplitude transmittance has radial symmetry. Furthermore, the half-width of the radially symmetric, hyper Gaussian masks can be controlled by changing the rotation angle β. This general result is illustrated for the particular case of $n = 2$, in Fig. 8.21.

Along the first line, of Fig. 8.21, we show the 3-D amplitude distributions of the transmittances in Eqs. (8.47), (8.48) and (8.49) respectively. Along the second line, of Fig. 8.21, we show the amplitude variations as 2-D color encoded pictures. It is interesting to note that the product of the asymmetrical masks in the first and second columns, of Fig. 8.21, generates the symmetrical masks shown at the third column of Fig. 8.21.

Finally, we emphasize on the many possibilities of this procedure by using the illustrations in Fig. 8.22. Along the first line we display the 1-D amplitude profiles of a sub Gaussian mask, $n = 1.5$, a Gaussian mask, $n = 2$, and super Gaussian mask, $n = 8$. The amplitude variations of these amplitude masks are shown as 2-D pictures along the second line of Fig. 8.22. Along the third line, of the same figure, we display 3-D curves.

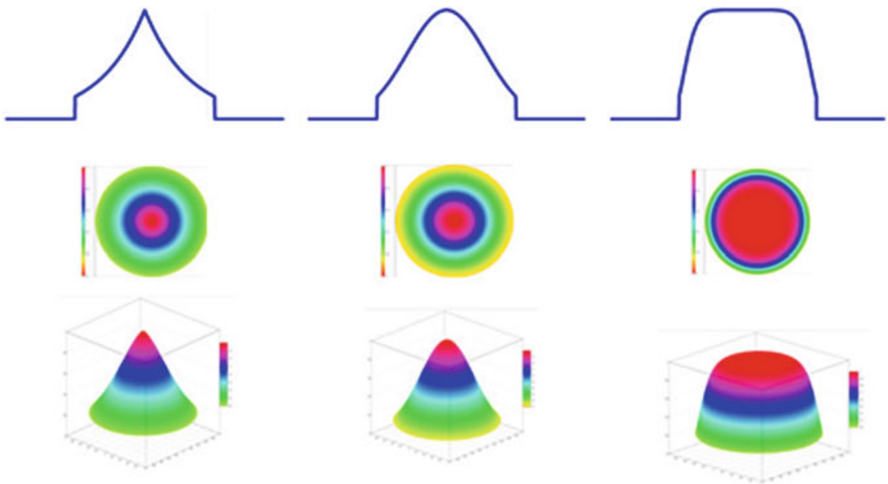

Fig. 8.22 Radially symmetric hyper Gaussian apodizer with tunable half-widths, which were generated by using a pair of masks that have helical amplitude variations

It is apparent from Eq. (8.49) and from Figs. 8.21 and 8.22 that by using a proper pair of masks, which have helical amplitude variations, one can control the half-width of a rather large set of hyper Gaussian masks. Of course, in principle one can extend the previous results to other types of apodizers.

8.5 Final Remarks

We have indicated that one can employ a rather simply optical processor for visualizing, as a 2-D picture, the evolution of a 2-D scalar wave; as is predicted by Helmholtz equation. For this type of application, one needs to use a very narrow slit that follows a semicircle over an otherwise opaque mask.

Then, we have noted that within the paraxial regime, Helmholtz equation has a different expression. Hence, for visualizing the evolution of the point spread function with focus error, one needs to use a very narrow slit that follows now a parabolic curve.

The above results were extended for visualizing the influence that the optical path difference (of certain phase mask) has over the point spread function of an optical system. We have discussed the use of another optical processor for obtaining displays that describe the impact of the optical path difference over the modulation transfer function.

Then, we have discussed the use of anamorphic processors for visualizing the generation of the ambiguity function of a 1-D pupil mask. We have related this method with the visualization of the optical transfer function with variable focus errors. When analyzing nonconventional devices using the ambiguity function, it is convenient to take into account the results obtained using the narrow slits.

Next, we have noted that the mathematical tools employed for describing the ambiguity function have a physical counterpart when using two refractive elements forming a pair, for implementing varifocal lenses; here denoted as Alvarez-Lohmann lenses. We have shown that the Alvarez-Lohmann lenses have an equivalent, when setting Gaussian apodizers with variable half-width.

We have indicated that the use of a pair of refractive elements, for controlling the optical power of a lens, leads to optical elements with helical phase variations. We have shown that one can control the optical path difference of a wide range of radial focalizers, if one uses a pair of refractive elements that have both helical phase variations and radial phase variations. To this end, one introduces an in-plane rotation between the refractive elements of the pair.

Finally, based on the previous results, we have discussed the use of two masks that have helical and radial amplitude variations for setting a large set of hyper Gaussian apodizers, with tunable half-width. Again for this application, one needs to introduce an in-plane rotation between the amplitude elements of the pair.

Acknowledgements We gratefully acknowledge the financial support of CONACYT, grant 157673, Fondo: I0017, as well as the grant 1477-CIO-UG-2013, DAIP, University of Guanajuato.

References

1. Jacquinot, P.: Apodization, Appendix E, in concepts of classical optics, John Strong, pp. 410–418. W. H. Freeman, San Francisco (1958)
2. Marechal, A., Françon, M.: Diffraction Structure Des Images, pp. 152–155. Masson, Paris (1970)
3. Papoulis, A.: Systems and Transforms with Applications in Optics, pp. 442–444. McGraw-Hill, New York (1968)
4. Steel, W.H.: Interferometry, pp. 23, 234, 248–249. Cambridge University Press, Cambridge (1983)
5. Goodman, J.W.: Introduction to Fourier Optics, pp. 151–154. McGraw-Hill, New York (1996)
6. Ojeda-Castañeda, J., Berriel-Valdos, L.R., Montes E.: Bessel annular apodizers: imaging characteristics. Appl. Opt. **26**(10), 2770–2772 (1987)
7. McCutchen, C.W.: Generalized aperture and three-dimensional diffraction image. J. Opt. Soc. Am. **54**(2), 240–244 (1964)
8. Ojeda-Castañeda, J., Berriel-Valdos, L.R.: Arbitrarily high focal depth with finite apertures. Opt. Lett. **13**(3), 183–185 (1988)
9. Ojeda-Castañeda, J., Andres, P., Diaz, A.: Strehl ratio with low sensitivity to spherical aberration. J. Opt. Soc. Am. A **5**(8), 1233–1236 (1988)
10. Ojeda-Castañeda, J., Tepichin, E., Pons, A.: Apodization of annular apertures: Strehl ratio. Appl. Opt. **27**(24), 5140–5145 (1988)
11. Mino, M., Okano, Y.: Improvement in the OTF of a defocused optical system through the use of shaded apertures. Appl. Opt. **10**(10), 2219 (1971)
12. Hauesler, G.: A method to increase the depth of focus by two step image processing. Opt. Commun. **6**(1), 38–42 (1972)
13. Chung, C.S., Hopkins, H.H.: Influence of nonuniform amplitude on the optical transfer function. Appl. Opt. **28**(6), 90–91 (1989)

14. Ojeda-Castañeda, J., Yépez-Vidal, E., Gómez-Sarabia, C.M.: Multiple-frame photography for extended depth of field. Appl. Opt. **52**(10), D84–D90 (2013)
15. Lohmann, A.W., Ojeda-Castañeda, J., Serrano-Heredia, A.: Trading dimensionality in signal processing. Opt. Laser Technol. **28**(2), 101–107 (1996)
16. Ojeda-Castañeda, J., Lohmann, A.W.: Young's experiment in signal synthesis, Chapter 14, Trends in Optic, Anna Consortini Editor, pp. 263–280. Academic Press, San Diego (1996)
17. Lohmann, A.W., Ojeda-Castañeda, J., Frausto, C.: Optical simulation of free-space propagation. Opt. Commun. **157**(1–6), 7–12 (1998)
18. Ojeda-Castañeda, J., Castro, A.: Simultaneous Cartesian coordinate display of defocused optical transfer functions. Opt. Lett. **23**(13), 1049–1051 (1998)
19. Woodward, P.M.: Radar ambiguity analysis, Technical Note No. 731. Royal Radar Establishment, London (1967)
20. Papoulis, A.: Ambiguity function in Fourier optics. J. Opt. Soc. Am. **64**(6), 779–788 (1974)
21. Guigay, J.P.: The ambiguity function in diffraction and isoplanatic imaging by partially coherent beams. Opt. Commun. 26(2), 136–138 (1978)
22. Marks, R.J., Walkup, J.K., Krile, T.F.: Ambiguity function display: an improved coherent processor. Appl. Opt. **16**(3), 746–750 (1977)
23. Brenner, K.-H., Lohmann, A.W., Ojeda-Castañeda, J.: The ambiguity function as a polar display of the OTF. Opt. Commun. **44**(5), 323–326 (1983)
24. Ojeda- Castañeda, J., Berriel-Valdos, L.R., Montes, E.: Ambiguity function as a design tool for high focal depth. Appl. Opt. **27**(4), 790–795 (1988)
25. Ojeda-Castañeda, J., Noyola-Isgleas, A.: High focal depth by apodization and digital restoration. Appl. Opt. **27**(12), 2583–2586 (1988)
26. Dowski, E.R., Cathey, T.W.: Extended depth of field through wave-front coding. Appl. Opt. **34**(11), 1859–1865 (1995)
27. Cook, C. E., Bernfeld, M.: Radar Signals: An Introduction to Theory and Applications, pp. 59–108. Arctech House, Norwood (1993)
28. George, N., Chi, W.: Extended depth of field using a Logarithmic asphere. J. Opt. Pure Appl. **5,** s157–s163 (2003)
29. Muyo, G., Harvey, A.R.: Decomposition of the optical transfer function: wavefront coding imaging systems. Opt. Lett. **30**(20), 2715–2717 (2005)
30. Sauceda-Carvajal, A., Ojeda-Castañeda, J.: High focal depth with fractional-power wave fronts. Opt. Lett. **29**(6), 560–562 (2004)
31. Castro, A., Ojeda-Castañeda, J.: Asymmetric phase masks for extended depth of field. Appl. Opt. **43**(17), 3474–3479 (2004)
32. Ojeda-Castañeda, J.: Focus error operator and related special functions. J. Opt. Soc. Am. **73**(8), 1042–1047 (1983)
33. Ojeda-Castañeda, J., Boivin, A.: The influence of wave aberrations: an operator approach. Can. J. Phys. **63**(2), 250–253 (1985)
34. Ojeda-Castañeda, J., Noyola-Isgleas, A.: Differential operator for scalar wave propagation. J. Opt. Soc. Am. A **5**(10), 1605–1609 (1988)
35. Ojeda-Castañeda, J., Berriel-Valdos, L.R., Montes, E.: Ambiguity function as a design tool for high focal depth. Appl. Opt. **27**(4), 790–795 (1988)
36. Marks, R.J. II, Walkup, J.K., Krile, T.F.: Ambiguity function display: an improved coherent processor. Appl. Opt. **16**(3), 746–750 (1977)
37. Castro, A., Ojeda-Castañeda, J., Lohmann, A.W.: Bow-tie effect: differential operator. Appl. Opt. **45**(30), 7878–7884 (2006)
38. Ojeda-Castañeda, J., Yépez-Vidal, E., García-Almanza, E.: Complex amplitude filters for extended depth of field. Photonics Lett. Pol. **2,** 162–164 (2010)
39. Ojeda-Castañeda J., Ledesma S. and Gomez-Sarabia C. M., Hyper Gaussian Windows with fractional wavefronts. Photonics Lett. Pol. **5**(1), 23–25 (2013)
40. Brenner, N., Rader, C.: IEEE Acoustics. Speech Signal Process. **24,** 264–266 (1976)
41. Plummer, W.T., Baker, J.G., van Tassell, J.: Photographic optical systems with nonrotational aspheric surfaces. Appl. Opt. **38**(16), 3572–2592 (1999)

42. Kitajima, I.: "Improvement in lenses". British Patent 250, 268 (July 29, 1926)
43. Lohmann, A.W.: Lente a focale variabili. Italian Patent 727, 848 (June 19, 1964)
44. Lohmann, A.W.: Improvements relating to lenses and to variable optical lens systems formed for such a lens. Patent Specification 998,191, London (1965)
45. Lohmann, A.W.: A new class of varifocal lenses. Appl. Opt. **9**(7), 1669–1671 (1970)
46. Alvarez, L.W.: Two-element variable-power spherical lens. US Patent 3, 305, 294 (December 3, 1964)
47. Alvarez, L.W., Humphrey, W.H.: Variable power lens and system. US Patent 3, 507, 565 (April 21, 1970)
48. Ojeda-Castañeda, J., Landgrave, J.E.A., Gómez-Sarabia, C.M.: The use of conjugate phase plates in the analysis of the frequency response of optical systems designed for an extended depth of field. Appl. Opt. **47**(22), E99–E105 (2008)
49. Ojeda-Castañeda, J., Aguilera Gómez, E., Plascencia Mora, H., Torres Cisneros, M., Ledesma Orozco, E.R., León Martínez, A., Pacheco Santamaría, J.S., Martínez Castro, J.G.: Carlos Salas Segoviano R., U. S. Patent 8, 159, 573B2 (April 17, 2012)
50. Ojeda-Castañeda, J., Gómez-Sarabia, C.M.: Key concepts for extending the depth of field with high resolution. Opt. Pura Apl. **45**(4) 449–459 (2012)
51. Ojeda-Castañeda, J., Yépez-Vidal, E., García-Almanza, E., Gómez-Sarabia, C.M.: "Tunable Gaussian mask for extending the depth of field". Photonics Lett. Pol. **4**(3), 115–117 (2012)
52. Lohmann, A.W., Paris, D.P.: "Variable Fresnel Zone Pattern" Appl. Opt. **6**(9), 1567–1570 (1967)
53. Burch, J.M., Williams, D.C.: Varifocal moiré zone plates for straightness measurement. Appl. Opt. **16**(9), 2445–2450 (1977)
54. Bernet, S., Jesacher, A., Fuerhapter, S., Maurer, C., Ritsch-Marte, M.: "Quantitative imaging of complex samples by spiral phase contrast microscopy". Opt. Express **14**(9) 3792–3805 (2006)
55. Jesacher, A., Fürhapter, S., Bernet, S., Ritsch-Marte, M.: "Spiral interferogram analysis". J. Opt. Soc. Am. A **23**(6) 1400–1409 (2006)
56. Bernet, S., Ritsch-Marte, M.: "Optical device with a pair of diffractive optical elements". US Patent 0134869 A1 (June 3, 2010)
57. Ojeda-Castañeda, J., Ledesma, S., Gomez-Sarabia, C.M.: Tunable apodizers and tunable focalizers using helical pairs. Photonics Lett. Pol. **5**(1), 20–22 (2013)
58. Ojeda-Castañeda, J., Gomez-Sarabia, C.M., Ledesma, S.: Tunable focalizers: axicons, lenses and axilenses, Tribute to H. John Caulfield, SPIE Proceedings 8833, 88330601–88330606 (2013)
59. Bryngdahl, O.: Radial- and circular-fringe interferograms. J. Opt. Soc. Am. **63**(9), 1098–1104 (1973)
60. Ojeda-Castañeda, J., Ledesma, S., Gomez-Sarabia, C.M.: Hyper Gaussian Windows with fractional wavefronts. Photonics Lett. Pol. **5**(1), 23–25 (2013)
61. Ojeda-Castañeda, J., Ledesma, S., Gomez-Sarabia, C.M.: Helical apodizers for tunable hyper Gaussian masks, Novel Optical System Design and Optimization XVI, SPIE Proceedings 8842, 88420N-1-88420N-6 (2013)

Index

O. Shulika, I. Sukhoivanov (eds.), *Advanced Lasers,*
Springer Series in Optical Sciences 193, DOI 10.1007/978-94-017-9481-7